Chemical Engineering Journal Advances 4 (2020) 100053

Contents lists available at ScienceDirect

Chemical Engineering Journal Advances

journal homepage: www.elsevier.com/locate/ceja

Hierarchical SnS_2/carbon nanotube@reduced graphene oxide composite as an anode for ultra-stable sodium-ion batteries

Yu Sun[a,1], Yanling Yang[a,1,*], Xiao-Lei Shi[b,c,1], Guoquan Suo[a], Huajun Chen[a,d], Muhammad Noman[a], Xinyong Tao[e,*], Zhi-Gang Chen[b,c,*]

[a] School of Materials Science and Engineering, Shaanxi Key Laboratory of Green Preparation and Functionalization for Inorganic Materials, Shaanxi University of Science and Technology, Xi'an 710021, PR China
[b] Centre for Future Materials, University of Southern Queensland, Springfield Central, QLD 4300, Australia
[c] School of Mechanical and Mining Engineering, The University of Queensland, QLD 4072, Australia
[d] Department of Environment and Chemistry, Luoyang Institute of Science and Technology, Luoyang 471023, PR China
[e] College of Materials Science and Engineering, Zhejiang University of Technology, Hangzhou 310014, China

ARTICLE INFO

Keywords:
SnS_2
Carbon nanotube
Reduced graphene oxide
Sodium-ion battery

ABSTRACT

Ultrathin SnS_2 layers with high theoretical specific capacity displays promising advantages as an anode in sodium storage systems. However, their poor conductivity and large capacity loss during charging/discharging process are urgently needed to be addressed. Herein, an exotic hierarchical SnS_2/carbon nanotube@reduced graphene oxide (SnS_2/CNT@rGO) composite has been designed and developed to be an anode for sodium-ion batteries. Functionally, the CNT penetrates into the petals of SnS_2 micro-flowers to increase the conductivity of SnS_2, while the three-dimensional rGO wraps around the SnS_2/CNT composite to relieve the volume expansion of SnS_2 during the charging/discharging process and construct "rGO conductive bridge" to accelerate electrode reaction kinetics. Benefiting from these exotic functionalization, the SnS_2/CNT@rGO anode possesses excellent reversible capacity and superior cycling stability with a high reversible capacity of 528 mA h g^{-1} at 50 mA g^{-1} and a retained capacity of 301 mA h g^{-1} after 1000 cycles at 1 A g^{-1}, which are better than most of the previously reported Sn-based and carbon-based anode materials. This study offers a promising strategy for significantly improving the cycling stability in the ultra-stable electrode materials in sodium-ion batteries.

1. Introduction

Concerns regarding to environmental pollution and energy crisis induced by burning of fossil fuels have significantly driven the advancement of renewable and sustainable energy. These renewable energy sources require more capable and inexpensive energy-storage technologies [1]. Currently, lithium-ion batteries (LIBs), including portable electronics, electric vehicles, and stationary storage devices, are supposed to be the main energy storage technology [2].Error! Reference source not found.Error! Reference source not found.Error! Reference source not found.Error! Reference source not found. Unfortunately, owing to the limitation and heterogeneity of global lithium resources, the cost of LIBs is sharply increasing [3]. Therefore, the searching for low-cost energy storage technology that uses natural and abundant materials has become a major trend. Recently, since sodium is earth abundant and low-cost, sodium-ion batteries (SIBs) show great potential as the alternatives to LIBs [4–6]. Compared with lithium ion, sodium ion has a large ionic radius and slow reaction kinetics, which causes greater polarization and volume expansion, leading to lower reversible capacity and poorer cycling stability [7]. Therefore, the cycling stability and specific capacity of SIBs is still needed to be enhanced to widen their practical applications.

Many studies have focused on the anode materials of SIBs, such as alloys and metals [8,9], oxides [10,11], and chalcogenides [12–14]. Particularly, layered transition-metal disulfides, such as MoS_2, WS_2, and SnS_2, have obtained considerable attention because of their high specific capacities [15]. SnS_2 comprises two closely packed layers of S atoms with Sn atoms between them, and adjacent S layers bounded *via* weak van der Waals interactions allow sodium (Na) ions to be de-intercalated and intercalated by using the conversion or alloying reaction with Na ions [16].

$$SnS_2 + 4Na = Sn + 2Na_2S \quad (1)$$

$$Sn + 3.75Na \leftrightarrow Na_{15}Sn_4 \quad (2)$$

* Corresponding authors.
E-mail addresses: yangyanling@sust.edu.cn (Y. Yang), tao@zjut.edu.cn (X. Tao), zhigang.chen@usq.edu.au (Z.-G. Chen).
[1] The first three authors contributed equally to this work.

https://doi.org/10.1016/j.ceja.2020.100053
Received 18 September 2020; Received in revised form 5 November 2020; Accepted 5 November 2020

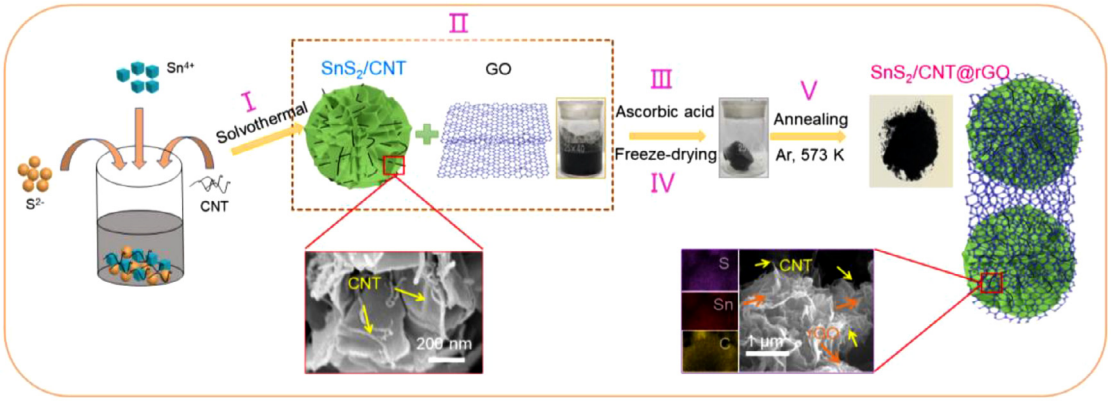

Fig. 1. Schematic illustration of the synthesis of SnS_2/CNT@rGO.

SnS_2 offers a high theoretical specific capacity (~1136 mA h g^{-1}), which is comparable to SnS and other transition-metal dichalcogenides such as WS_2 and MoS_2 [16]. Unfortunately, the significant volume change of SnS_2 caused by the alloying results in rapid decay of specific capacity and poor cycle stability [17]. In order to enhance the cycling stability of SnS_2 electrodes, various carbonaceous materials, such as expanded graphite [18,19], carbon nanofiber/nanoline [20,21], and porous carbon [22], have introduced into the anodes for enhancing the electrochemical activity of stored sodium ions. However, their specific capacity and cycle stability are still far to reach used level. Therefore, searching for new-type anode materials with high specific capacity and high cycle stability still remains a huge challenge in SIBs.

In this study, we develop a rational design of an exotic hierarchical SnS_2/carbon nanotube@reduced graphene oxide composite (SnS_2/CNT@rGO) *via* simple solvothermal method combined with annealing processes. Functionally, CNTs penetrate into the petals of SnS_2 micro-flowers to increase the conductivity of SnS_2, while the three-dimensional rGO wraps around the SnS_2/CNT composite to relieve the volume expansion of SnS_2 during the charging/discharging process and constructs "rGO conductive bridge" to accelerate electrode reaction kinetics. Such assembly strategy enables SnS_2/CNT@rGO anode possessing a high reversible capacity (528 mA h g^{-1} at 50 mA g^{-1}) and an ultra-stable cycling capacity with 301 mA h g^{-1} over 1000 cycles at 1 A g^{-1} for SIBs. After detailed structural and property analysis, we further illustrate the underlying physics and chemistry. Our work indicates that our hierarchical assembly strategy inspires more advanced electrode designs with improved internal conductivity and long-term cycle stability.

2. Experimental details

2.1. Materials

$SnCl_4 \bullet 5H_2O$, Hexadecyl trimethyl ammonium Bromide (CTAB), thioglycolic acid ($C_2H_4O_2S$), ascorbic acid and polyvinyl alcohol (PEG 200) were purchased from Shanghai McLean Biochemical Co., Ltd. All reagents were used to prepare SnS_2 of analytical grade, no additional purification was required.

2.2. Preparation of SnS_2/CNT composite

For a typical process, 0.02 g of CNT, 0.4655 g of $SnCl_4 \bullet 5H_2O$, 0.35 g of CTAB, and 0.2579 g of thioglycolic acid were added to 30, 20, 30, and 20 mL of PEG 200, respectively, and was magnetically stirred for 30 min. $SnCl_4 \bullet 5H_2O$ solution was mixed with CTAB solution followed by ultrasonication for 5 min, and then the solution was mixed with the above thioglycolic acid solution and CNT solution with magnetically stirring for 1 h. Once all precursors were dissolved, the stirred solution was poured into a 200 mL polytetrafluoroethylene reactor and placed in an oven at 200 °C for 10 h. Then, the autoclave was cooled to 60 °C in the oven. The SnS_2/CNT product was centrifugated and washed by using standard methods, and dried at 60 °C. In this study, the process to synthesize pure SnS_2 was similar to the method just described.

2.3. Synthesis of SnS_2/rGO and SnS_2/CNT@rGO composite

Dried SnS_2/CNT composite (1.5 g) was dispersed into a GO solution (10 mL, 3 mg mL^{-1}) and magnetically stirred for 5 h. Then, ascorbic acid (0.3 g) was dispersed into the mixture. After that, the mixture was placed in an oven at 90 °C for 3 h and thus a SnS_2/CNT@rGO composite gel was acquired. Then, the above gel was freeze-dried using a vacuum freeze-dryer and further calcined at 573 K in argon (Ar) for 5 h, forming a powdery hierarchical SnS_2/CNT@rGO composite. The synthesis process of SnS_2/rGO is similar to SnS_2/CNT@rGO composite, except that the SnS_2/CNT composite is replaced with pure SnS_2.

2.4. Materials characterization

The structural characteristics of materials were characterized by using X-ray diffraction (XRD, D/max2200PC, Cu Kα), X-ray photoelectron spectroscopy (XPS, AXIS SUPRA), and Raman spectroscopy (Renishaw-invia). The morphology of the composite was analyzed using transmission electron microscopy (TEM, FEI Tecnai G2 F20 S-TWIN) and field-emission scanning electron microscopy (FEI, Verios 460, 2 kV accelerating voltage).

2.5. Electrochemical characterization

Firstly, the slurry was fabricated by mixing 10 wt.% polyvinylidene fluoride binder, 70 wt.% active materials (SnS_2, SnS_2/CNT, SnS_2/rGO and SnS_2/CNT@rGO) and 20 wt.% super P dissolved in N-methyl-2-pyrrolidinone on copper foil. After that, a doctor blade with a thickness of about 100 μm was used to apply the slurry to the copper foil and vacuum dry at 80 °C for 10 h. Finally, the film on the copper foil was cut into a disc with a diameter of 12 mm and an active material loading of 0.3–1 mg cm^{-2} as an electrode. The specific capacity of the electrode was calculated based on the mass of the active material. CR2032 coin cells with sodium metal were used to elucidate the electrochemical performance of electrodes, and the SnS_2/CNT@rGO composite was punched into 10-mm-diameter disks to use as working electrodes. The coin cells were assembled into a half-battery in an Ar-filled glove box containing oxygen and moisture concentrations maintained below 1 ppm. 1 M $NaPF_6$ electrolyte solution was dissolved in dimethyl carbonate (DMC) and ethylene carbonate (EC) solution with a volume ratio of 1:1. The room-temperature electrochemical characterizations were measured in the LAND test system.

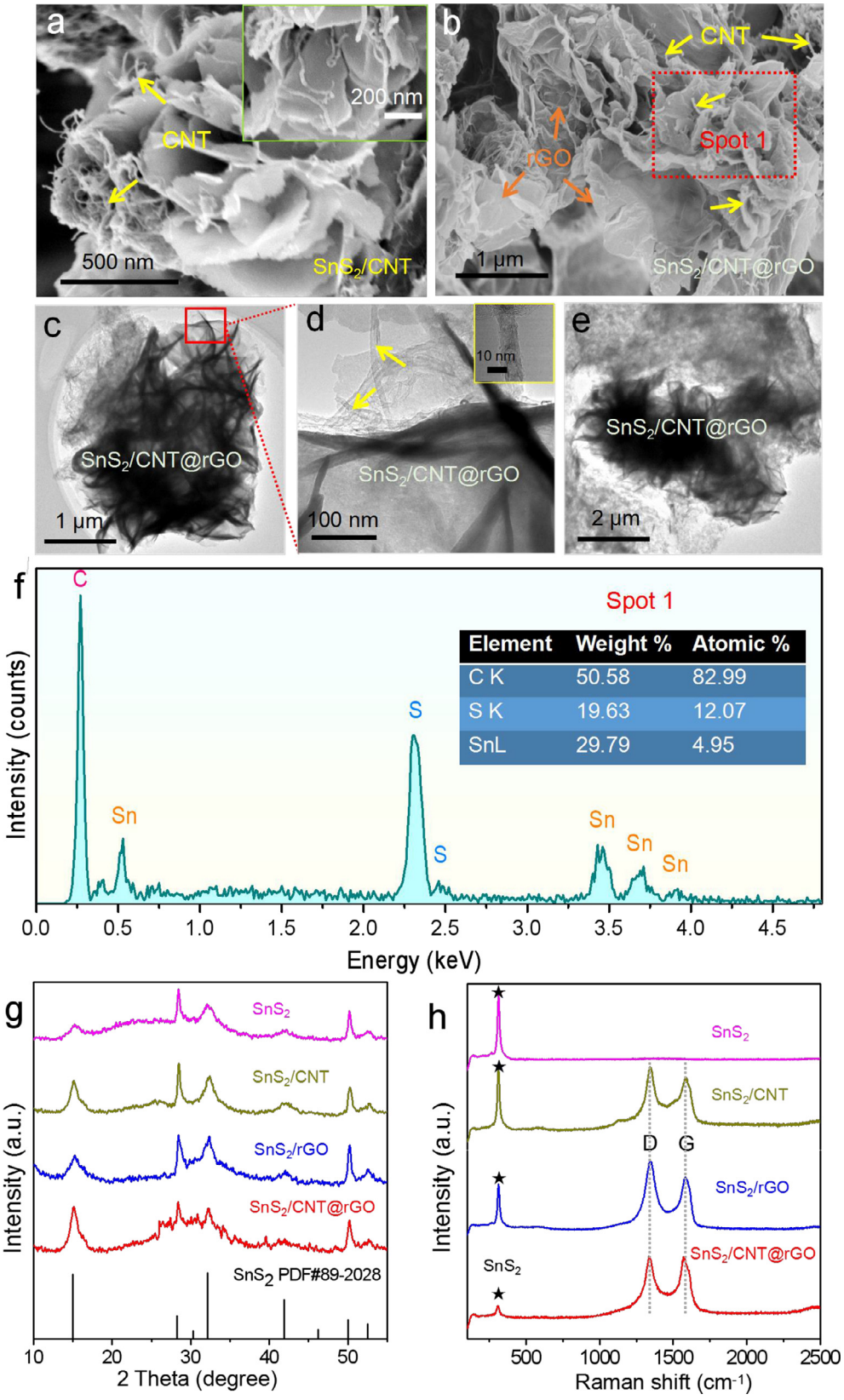

Fig. 2. SEM images of (a) SnS_2/CNT (the illustration is an enlarged view of the local SnS_2/CNT) and (b) SnS_2/CNT@rGO; (c-e) TEM images of SnS_2/CNT@rGO; (f) EDX spectrum of SnS_2/CNT@rGO; (g) XRD patterns of SnS_2, SnS_2/CNT, SnS_2/rGO and SnS_2/CNT@rGO; (h) Raman spectrum of SnS_2, SnS_2/CNT, SnS_2/rGO and SnS_2/CNT@rGO.

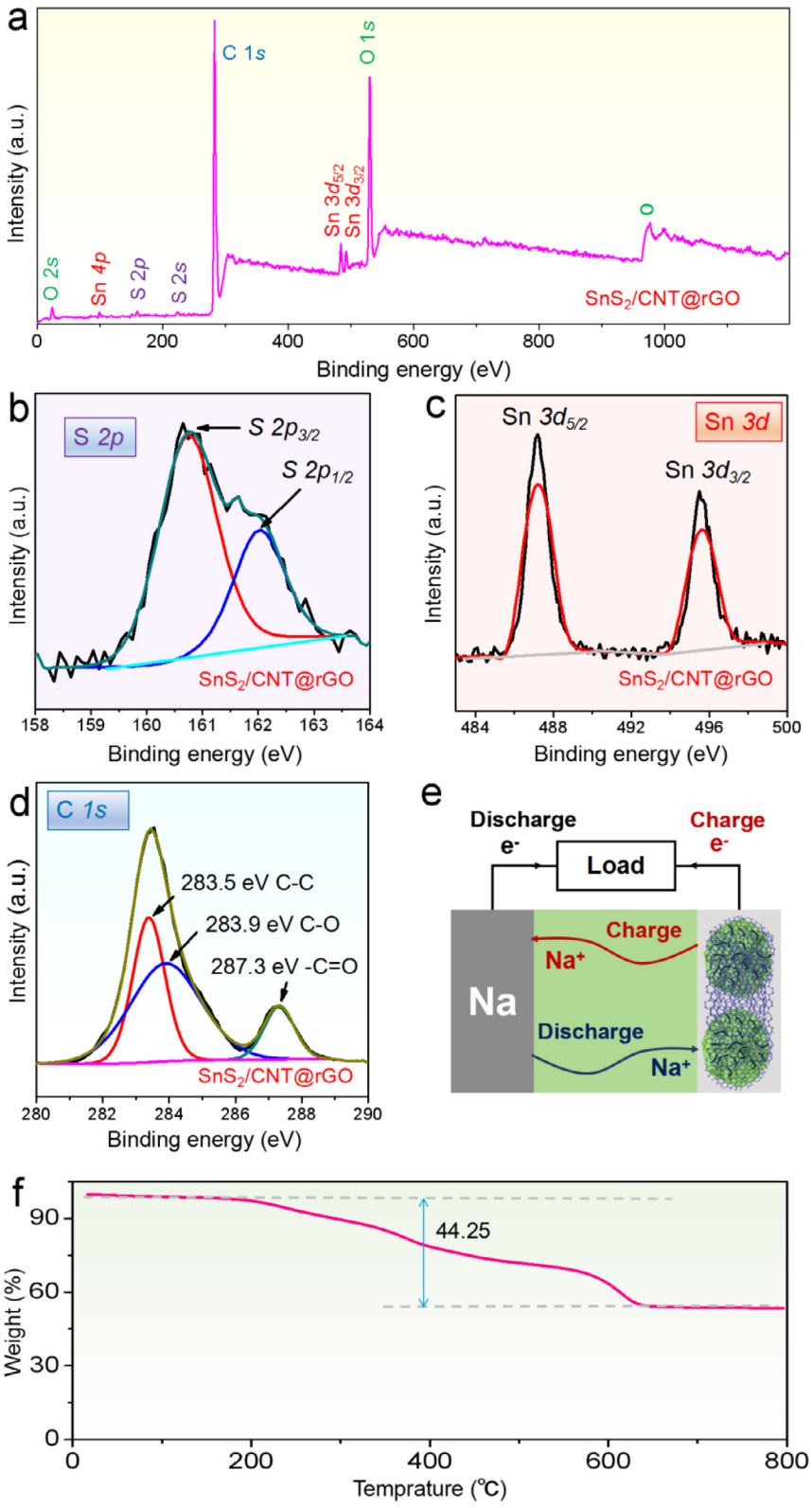

Fig. 3. (a) Survey, (b) S *2p*, (c) Sn *3d*, and (d) C *1s* XPS spectra of the SnS_2/CNT@rGO composite; (e) Schematic diagram of the Na-ion battery designed in this work; (f) TGA of the prepared SnS_2/CNT@rGO composite room temperature to 800 ˚C in the air.

3. Results and discussion

In order to understand our strategy for the synthesis of hierarchical SnS_2/CNTs@rGO composite, we schematically plot our procedure as shown in Fig. 1. As can be seen, CNTs are firstly sonicated to uniformly disperse in the PEG 200. The tin source, sulfur source, CTAB and CNTs are mixed and subjected to solvothermal treatment to prepare SnS_2/CNTs. Secondly, SnS_2/CNTs powder and GO aqueous solution are mixed and stirred for hours. Thirdly, ascorbic acid was added into the solution and then was placed in an oven at 90 ˚C for 3 h to acquire SnS_2/CNT@rGO composite gel. After that, the gel was freeze-dried using a vacuum freeze-dryer to maintain the hierarchical structure. At last, the freeze-dried block was further annealed at 573 K in argon (Ar) for 5 h to improve the crystallinity, forming a powdery

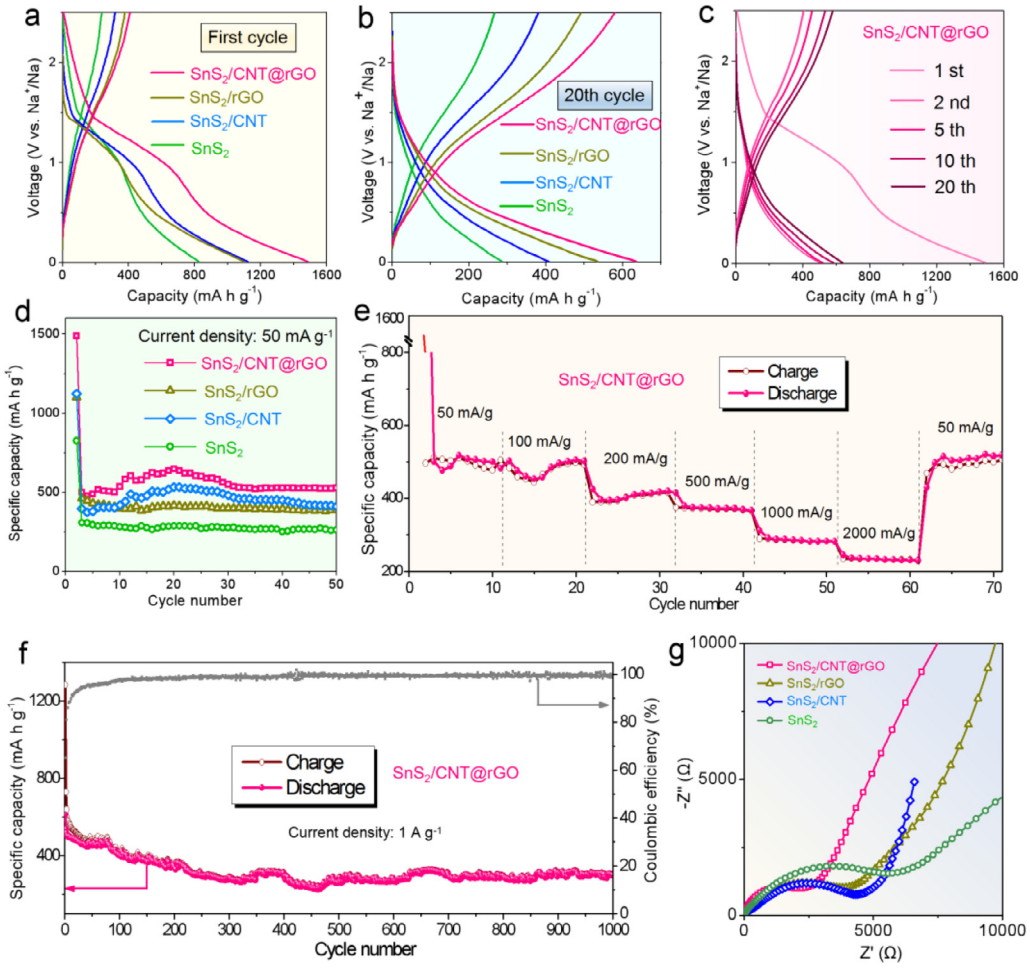

Fig. 4. (a, b) Initial galvanostatic and twentieth galvanostatic charge-discharge curves of SnS_2, SnS_2/CNT, SnS_2/rGO and SnS_2/CNT@rGO at 50 mA g^{-1}; (c) Charge and discharge curves of SnS_2/CNT@rGO at 50 mA g^{-1}; (d) Cycling stability of SnS_2, SnS_2/CNT, SnS_2/rGO and SnS_2/CNT@rGO at 50 mA g^{-1}; (e) Rate properties of SnS_2/CNT@rGO; (f) Cycling stability of SnS_2/CNT@rGO at 1 A g^{-1} over 1000 cycles; (g) Nyquist plots of SnS_2, SnS_2/CNT, SnS_2/rGO and SnS_2/CNT@rGO.

hierarchical SnS_2/CNT@rGO composite. It should be pointed out that the hierarchical SnS_2/CNT@rGO composite has a well-interconnected microstructure and enough electron transport channels.

Fig. 2 shows the typical morphological and structural characteristics of the fabricated SnS_2/CNT and SnS_2/CNT@rGO composite. Fig. 2**a** is a typical SEM image of SnS_2/CNT. As can be seen, well-defined SnS_2 micro-flowers has a size ranging from 1 to 2 μm. CNT with short length can be inserted between petals, as illustrated in Fig. 2**a**. In addition, SnS_2 micron petals have more space to accommodate the presence of partially agglomerated CNTs, as shown in Fig. 2**a**. Particularly, the CNTs penetrates into the petals of SnS_2 micro-flowers. It should be noted that the bonding strength between CNTs and SnS_2 petals is weak, which may induce that the CNTs separate from the SnS_2 petals because of the volume change during charging and discharging processes. In order to alleviate the potential separation, atomic-level graphene nanosheets with excellent flexibility and conductivity are further introduced to encapsulate SnS_2/CNT to form SnS_2/CNT@rGO composite. Its typical SEM image is shown in Fig. 2**b**, which reveals that the graphene network well wrapped around the SnS_2/CNT. TEM was further used to characterize the structural characteristics of the SnS_2/CNT@rGO composite and its typical TEM images are shown in Fig. 2**c-e.** As can be seen, CNTs intertwine with rGO and cohere to SnS_2 petals. These CNTs can improve the internal conductivity of SnS_2, and graphene sheets encapsulated on SnS_2/CNT also constitute a conductive network. Furthermore, the flexible graphene network provides space for releasing the volume expansion during charging and discharging processes. Energy-dispersive X-ray microanalysis (EDX) of Fig. 2**f** is employed to determine the element distribution at the point marked in Fig. 2**b**. The results reveal the presence of elemental S, C, and Sn in the composite.

The crystalline structures of SnS_2, SnS_2/CNT, SnS_2/rGO and SnS_2/CNT@rGO were examined by XRD and their corresponding diffraction patterns are shown in Fig. 2**g**. All the main diffraction peaks can be assigned to 2T-type hexagonal SnS_2 (PDF: 89-2028) [23] for these three samples. Moreover, a weak peak at 26° and a broad peak at 22°–28° for SnS_2/CNT@rGO can be observed, which indicate the presence of crystalline carbon [24,25]. Raman spectroscopy was used to further characterize the SnS_2, SnS_2/CNT, SnS_2/rGO and SnS_2/CNT@rGO and the results are shown in Fig. 2**h**. The *D* and *G* bands appear at 1357 cm^{-1} and 1595 cm^{-1}, which indicate the presence of carbon in composites [26]. The peaks centered at 281–355 cm^{-1} are all attributed to SnS_2 [27]. The Raman intensity of SnS_2 in SnS_2/CNT@rGO is low, which should be ascribed to the surface coverage by rGO, which indicates that SnS_2 has sufficient contact with the rGO network [28].

Fig. 3 shows the chemical states of SnS_2/CNT@rGO investigated by XPS. Fig. 3**a** is a full XPS spectrum of SnS_2/CNT@rGO, in which Sn, S, and C peaks can be clearly seen. Fig. 3**b** illustrates the high-resolution S 3*p* spectrum of SnS_2/CNT@rGO, and two strong peaks at 160.9 and 162.0 eV correspond to S $2p_{3/2}$ and S $2p_{1/2}$ of S^{2-} in SnS_2 [29]. The spectrum of Sn 3*d* in Fig. 3**c** contains peaks indicative to the Sn $3d_{5/2}$ and $3d_{3/2}$ states at 487.1 and 495.4 eV [30]. The *C 1s* spectrum of Fig. 3**d** is decomposed into three peaks at 283.3, 283.9, and 287.3 eV, which can be assigned to graphite C–C, C–O, and C=O,

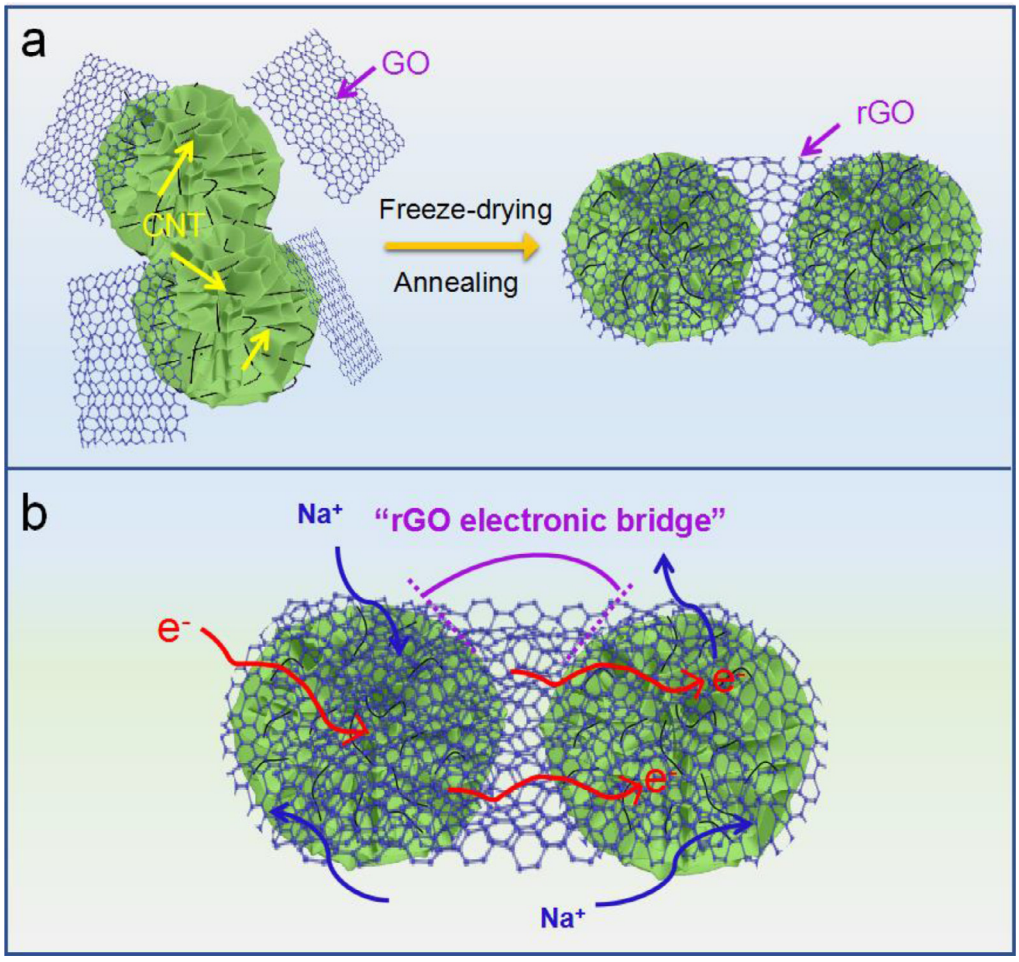

Fig. 5. (a) Schematic illustrating the formation of the SnS_2/CNT@rGO composite; (b) The schematic diagram illustrates the high storage capacity and electron transport path of sodium ions in SnS_2/CNT@rGO.

respectively [31,32]. It should be mentioned that SnS_2 and rGO are tightly connected by our heat treatment [33]. On the basis of these chemical states of SnS_2/CNT@rGO composite, we schematically design the anode electrode operating mechanism when the SnS_2/CNT@rGO composite material is used as anode in SIBs, as illustrated in **Fig. 3e**. The related electrochemical performance was examined in the half-cell where Na metal serves as a counter electrode. The SnS_2/CNT@rGO composite was further analyzed by TGA in the air from room temperature to 800 °C, as shown in **Fig. 3f**. The TGA chart shows that the decomposition of rGO and CNT and the oxidation of SnS_2 to SnO_2 result in weight loss between 400 °C and 640 °C [34]. TGA results show that the composite contains about 46.0 % of SnS_2 and 54.0% of rGO and CNT by weight.

To verify our advantages of the exotic network microstructure of SnS_2/CNT@rGO, CR2032 coins were fabricated by using our SnS_2/CNT@rGO composite and the measured results are plotted in **Fig. 4**. **Fig. 4a-b** illustrate the initial and the twentieth galvanostatic charge-discharge curves for SnS_2, SnS_2/CNT, SnS_2/rGO and SnS_2/CNT@rGO electrodes between 0.01 and 3.0 V versus Na^+/Na at 50 mA g^{-1} current density. Obviously, the charge-discharge characteristics and capacities of the three electrodes are different. The initial charge capacities of SnS_2, SnS_2/CNT, SnS_2/rGO and SnS_2/CNT@rGO at 50 mA g^{-1} are 825, 1100, 1100.1 and 1488 mA h g^{-1}, associated with the initial coulombic efficiencies of 29.6 %, 35.3 %, 35.4 % and 28.3 %, respectively. The twentieth charge capacities of SnS_2, SnS_2/CNT and SnS_2/rGO, SnS_2/CNT@rGO at 50 mA g^{-1} are 285, 535, 534.6 and 1488 mA h g^{-1}, associated with the twentieth coulomb efficiencies of 96.6 %, 94.9 %, 94.8 % and 94.2 %, respectively. Compared with the initial coulombic efficiencies, the twentieth coulombic efficiencies increase by 67 %, 59.6 %, 59.4 % and 65.9 %, respectively. Obviously, SnS_2/CNT@rGO anode shows increased coulombic efficiencies with increasing the numbers of cycles.

Fig. 4c compares the electrochemical performance of SnS_2/CNT@rGO at different numbers of charge-discharge cycles. At 50 mA g^{-1}, SnS_2/CNT@rGO has a specific capacity of 1488, 501, 518, 582 and 636 mA h g^{-1} and a coulombic efficiency of 28 %, 83 %, 91 %, 94 % and 94 % for the first, second, fifth, tenth and twentieth cycle, respectively. These results suggest that the SnS_2/CNT@rGO electrode gradually stabilizes with increasing the number of cycles. **Fig. 4d** plots the cycling properties of the SnS_2, SnS_2/CNT, SnS_2/rGO and SnS_2/CNT@rGO electrodes at 50 mA g^{-1}. Obviously, the performance of the SnS_2/CNT@rGO is much superior to that of the SnS_2, SnS_2/CNT and SnS_2/rGO. Due to the electrochemical activation of SnS_2 by the CNTs in the petals, the capacity of the SnS_2/CNT and SnS_2/CNT@rGO electrode increases slightly in the first 20 cycles. In the next 10 cycles, due to the volume expansion, a part of CNTs are released from the SnS_2 petals, and the capacity of the two decreases slightly. The capacity of SnS_2/rGO is slightly lower due to the poor conductivity of SnS_2. Compared with SnS_2 and SnS_2/CNT, SnS_2/rGO is more stable because rGO can inhibit the volume expansion of electrode during charging and discharging. After 50 cycles, the remaining specific capacity of the SnS_2, SnS_2/CNT and SnS_2/rGO is only 261, 440 and 389.2 mA h g^{-1}, whereas the SnS_2/CNT@rGO maintains a much higher specific capacity of 528 mA h g^{-1}. **Fig. 4e** shows the rate

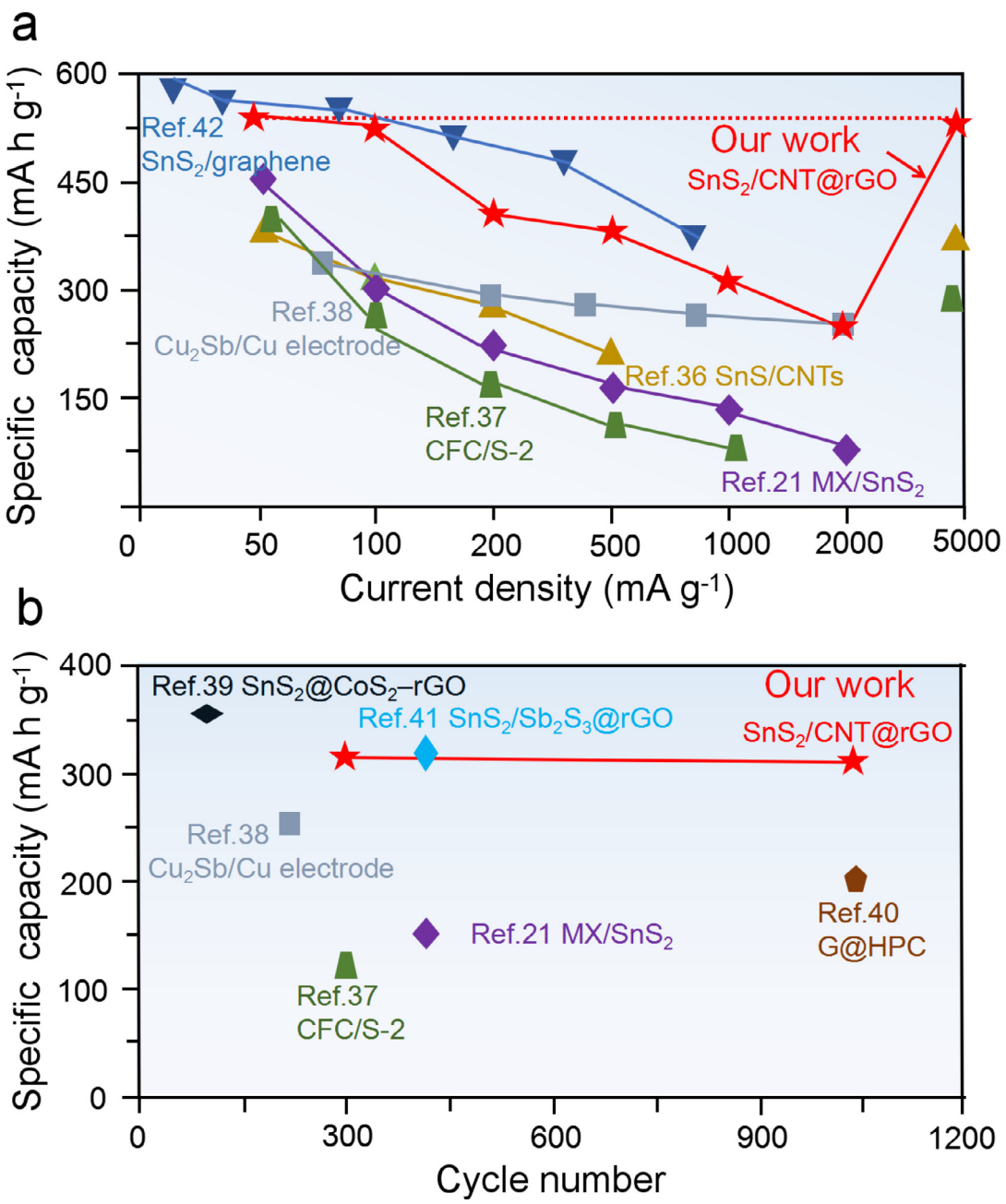

Fig. 6. Comparison of the evolution of specific capacity with (a) current density and (b) cycle number of Sn-based and C-based electrode materials (current density: 1 A g^{-1}) reported previously [16,36-42] with our work.

performance of SnS_2/CNT@rGO at different current densities. As can be seen, the SnS_2/CNT@rGO has a capacity of 510, 502, 420, 368, 282 and 230 mA h g^{-1} at a current density of 0.05, 0.1, 0.2, 0.5, 1 and 2 A g^{-1}, respectively. Upon suddenly switching the current density back to 50 mA g^{-1} subsequent to 60 cycles, the discharge capacity is restored to 519 mA h g^{-1}, which is almost equivalent to the original value, suggesting that the exotic network microstructure in the SnS_2/CNT@rGO composite remains intact after exposure to a transient current density. These results indicate that the SnS_2/CNT@rGO composite overcomes the problems of low conductivity and large volume change during charging and discharging processes of SnS_2. This superior specific capacity of SnS_2/CNT@rGO should be attributed to the unique network microstructure, which promotes the rapid diffusion of ions, endows SnS_2 with excellent conductivity and provides additional space for volume expansion.

Fig. 4**f** shows the evolution of specific capacity of SnS_2/CNT@rGO anode with increasing the cycle number. At a high current density of 1 A g^{-1} subsequent to 1000 cycles, the SnS_2/CNT@rGO anode still has a high specific capacity of 301 mA h g^{-1} and a high coulombic efficiency of 99.6 %. Moreover, the SnS_2/CNT@rGO anode exhibits extraordinary stability with a high retention of specific capacity, for instance of 98% from 400 to 1000 cycle. We applied electrochemical impedance spectroscopy (EIS) technology to determine the resistance to ion migration, as shown in Fig. 4**g**. ESI results show that the SnS_2/CNT@rGO electrode has a small charge-transfer resistance (Rct), indicating that the resistance of the solid interface layer is lower than that of pure SnS_2, SnS_2/CNT and SnS_2/rGO. SnS_2 has a smaller particle contact resistance, which is conducive to the transmission of Na^+ [35]. This can be attributed to the addition of CNT and rGO, which greatly improves the electronic conductivity of the layered structure.

In order to further understand our excellent cycle stability and specific capacity of SnS_2/CNT@rGO anode, we build up the multistage structure of the SnS_2/CNT@rGO composite, as schematically illustrated in Fig. 5a. Firstly, at the electrode level, SnS_2/CNT units are combined together by rGO under high temperature treatment to form a hierarchical composite structure, which is essential for high specific capacity of the anode for SIBs. Secondly, the large SnS_2 petals can significantly reduce diffusion/migration barrier to enhance Na^+ insertion, and in turn enhance the utilization rate of active materials. Meanwhile, CNTs serve as good electron conductors in SnS_2/CNT@rGO, which are conducive to electron transmission. Thirdly, the rGO thus relieves volume expansion of the electrode and serves as a "bridge" to connect SnS_2/CNT units, which is conducive to electron transmission throughout the electrode, as schematically shown in Fig. 5b.

In order to compare the electrochemical performance between our SnS_2/CNT@rGO electrode and other SnS_2-based electrode materials reported previously, their evolutions of specific capacity with current density and cycle number are plotted in Fig. 6. Obviously, the cycle stability and specific capacity of our SnS_2/CNT@rGO electrode are superior than most of the previously reported Sn-based and C-based electrode materials. This should be attributed to the rapid electron transport ability and a great degree of relieving the volume expansion during charging and discharging of the network microstructure.

4. Conclusion

In summary, we use solvothermal and freeze-drying process combined with annealing to fabricate SnS_2/CNT@rGO composite with unique network structure for ultra-stable sodium-ion batteries. SnS_2/CNT units group together by rGO to form a hierarchical structure in SnS_2/CNT@rGO composite. The exotic structure not only effectively enhances the conductivity and relieves the material volume expansion during charging and discharging, but also builds an "rGO conductive bridge" to accelerate electron transport and improve electrode reaction kinetics. The obtained SnS_2/CNT@rGO composite, used as an anode of sodium-ion battery, shows excellent reversible capacity and superior cycling stability with a high reversible capacity of 528 mA h g^{-1} at 50 mA g^{-1} and a retained capacity of 301 mA h g^{-1} after 1000 cycles at 1 A g^{-1}, which are superior than most of the previously reported Sn-based and C-based electrode materials. Our study offers a promising path to significantly improve the cycling stability of SnS_2 and advance ultrahigh-stability electrode materials for sodium-ion batteries.

Declaration of Competing Interest

The authors declare that they have no known competing financial interests or personal relationships that could have appeared to influence the work reported in this paper.

Acknowledgments

The authors acknowledge financial support from the National Natural Science Foundation of China (Grant Nos.: 51464020, 51704188, 51802181, 61705125 and 51702199), Jiangxi Natural Science Foundation (Grant Nos.: 20161BAB206164 and 20161BBH80062), and Australian Research Council.

References

[1] A. Sarkar, C.V. Manohar, S. Mitra, A simple approach to minimize the first cycle irreversible loss of sodium titanate anode towards the development of sodium-ion battery, Nano Energy 70 (2020) 104520.
[2] H. Liu, Z. Zhu, Q. Yan, S. Yu, X. He, Y. Chen, R. Zhang, L. Ma, T. Liu, M. Li, R. Lin, Y. Chen, Y. Li, X. Xing, Y. Choi, L. Gao, H.S. Cho, K. An, J. Feng, R. Kostecki, K. Amine, T. Wu, J. Lu, H.L. Xin, S.P. Ong, P. Liu, A disordered rock salt anode for fast-charging lithium-ion batteries, Nature 585 (2020) 63–67.
[3] F. Wu, V. Srot, S. Chen, S. Lorger, P.A. van Aken, J. Maier, Y. Yu, 3D honeycomb architecture enables a high-rate and long-life iron (III) fluoride-lithium battery, Adv Mater 31 (2019) 1905146.
[4] B. Sun, P. Xiong, U. Maitra, D. Langsdorf, K. Yan, C. Wang, J. Janek, D. Schroder, G. Wang, Design strategies to enable the efficient use of sodium metal anodes in high-energy batteries, Adv Mater 32 (2020) 1903891.
[5] D. Xie, M. Zhang, Y. Wu, L. Xiang, Y. Tang, A flexible dual-ion battery based on sodium-ion quasi-solid-state electrolyte with long cycling life, Adv Funct Mater 30 (2019) 1906770.
[6] J.M. Lee, G. Singh, W. Cha, S. Kim, J. Yi, S.-J. Hwang, A. Vinu, Recent advances in developing hybrid materials for sodium-ion battery anodes, ACS Energy Lett 5 (2020) 1939–1966.
[7] D.M. Zhang, J.H. Jia, C.C. Yang, Q. Jiang, Fe_7Se_8 nanoparticles anchored on N-doped carbon nanofibers as high-rate anode for sodium-ion batteries, Energy Storage Mater 24 (2020) 439–449.
[8] H. Gu, L. Yang, Y. Zhang, C. Wang, X. Zhang, Z. Xie, J. Wei, Z. Zhou, Highly reversible alloying/dealloying behavior of SnSb nanoparticles incorporated into N-rich porous carbon nanowires for ultra-stable Na storage, Energy Storage Mater 21 (2019) 203–209.
[9] S. Liang, Y.J. Cheng, J. Zhu, Y. Xia, P. Müller-Buschbaum, A chronicle review of non-silicon (Sn, Sb, Ge)-based lithium/sodium-ion battery alloying anodes, Small Methods 4 (2020) 2000218.
[10] L. Wang, Z. Wei, M. Mao, H. Wang, Y. Li, J. Ma, Metal oxide/graphene composite anode materials for sodium-ion batteries, Energy Storage Mater 16 (2019) 434–454.
[11] S. Fang, D. Bresser, S. Passerini, Transition metal oxide anodes for electrochemical energy storage in lithium- and sodium-ion batteries, Adv Energy Mater 10 (2019) 1902485.
[12] H. Tan, Y. Feng, X. Rui, Y. Yu, S. Huang, Metal chalcogenides: paving the way for high-performance sodium/potassium-ion batteries, Small Methods 4 (2019) 1900563.
[13] Z. Ali, T. Zhang, M. Asif, L. Zhao, Y. Yu, Y. Hou, Transition metal chalcogenide anodes for sodium storage, Mater Today 35 (2020) 131–167.
[14] L. Wang, Q. Zhao, Z. Wang, Y. Wu, X. Ma, Y. Zhu, C. Cao, Cobalt-doping SnS_2 nanosheets towards high-performance anodes for sodium ion batteries, Nanoscale 12 (2020) 248–255.
[15] J. Chen, D.H.C. Chua, P.S. Lee, The advances of metal sulfides and in situ characterization methods beyond Li ion batteries: sodium, potassium, and aluminum ion batteries, Small Methods 4 (2019) 1900648.
[16] Y. Wu, P. Nie, L. Wu, H. Dou, X. Zhang, 2D MXene/SnS_2 composites as high-performance anodes for sodium ion batteries, Chem Eng J 334 (2018) 932–938.
[17] Z. Liu, A. Daali, G.L. Xu, M. Zhuang, X. Zuo, C.J. Sun, Y. Liu, Y. Cai, M.D. Hossain, H. Liu, K. Amine, Z. Luo, Highly reversible sodiation/desodiation from a carbon-sandwiched SnS_2 nanosheet anode for sodium ion batteries, Nano Lett 20 (2020) 3844–3851.
[18] Y. Jiang, D. Song, J. Wu, Z. Wang, S. Huang, Y. Xu, Z. Chen, B. Zhao, J. Zhang, Sandwich-like SnS_2/graphene/SnS_2 with expanded interlayer distance as high-rate lithium/sodium-ion battery anode materials, ACS Nano 13 (2019) 9100–9111.
[19] Z. Sang, X. Yan, D. Su, H. Ji, S. Wang, S.X. Dou, J. Liang, A flexible film with SnS_2 nanoparticles chemically anchored on 3D-graphene framework for high areal density and high rate sodium storage, Small 16 (2020) 2001265.
[20] Y. Wang, Y. Zhang, J. Shi, X. Kong, X. Cao, S. Liang, G. Cao, A. Pan, Tin sulfide nanoparticles embedded in sulfur and nitrogen dual-doped mesoporous carbon fibers as high-performance anodes with battery-capacitive sodium storage, Energy Storage Mater 18 (2019) 366–374.
[21] W. Yan, M. Li, H. Li, C. Li, S. Xu, L. Su, L. Qian, B. Yang, Aqueous lithium and sodium ion capacitors with boron-doped graphene/BDD/TiO_2 anode and boron–doped graphene/BDD cathode exhibiting AC line-filtering performance, Chem Eng J 388 (2020) 124265.
[22] D. Li, Q. Sun, Y. Zhang, L. Chen, Z. Wang, Z. Liang, P. Si, L. Ci, Surface-confined SnS_2@C@rGO as high-performance anode materials for sodium-and potassium-ion batteries, ChemSusChem 12 (2019) 2689–2700.
[23] C. Lin, M. Zhu, T. Zhang, Y. Liu, Y. Lv, X. Li, M. Liu, Cellulose/SnS_2 composite with enhanced visible-light photocatalytic activity prepared by microwave-assisted ionic liquid method, Rsc Adv 7 (2017) 12255–12264.
[24] J. Zhou, Y. Lan, K. Zhang, G. Xia, J. Du, Y. Zhu, Y. Qian, In-situ growth of carbon nanotubes wrapped Si composites as anodes for high performance lithium ion batteries, Nanoscale 8 (2016) 4903–4907.
[25] R. Kato, S. Igarashi, T. Umakoshi, P. Verma, Tip-enhanced raman spectroscopy of multiwalled carbon nanotubes through D-band imaging: implications for nanoscale analysis of interwall interactions, ACS Appl. Nano Mater. 3 (2020) 6001–6008.
[26] J. Liu, M. Zheng, X. Shi, H. Zeng, H. Xia, Amorphous FeOOH quantum dots assembled mesoporous film anchored on graphene nanosheets with superior electrochemical performance for supercapacitors, Adv Funct Mater 26 (2016) 919–930.
[27] Y. Chen, X. Li, K. Park, W. Lu, C. Wang, W. Xue, F. Yang, J. Zhou, L. Suo, T. Lin, H. Huang, J. Li, J.B. Goodenough, Nitrogen-doped carbon for sodium-ion battery anode by self-etching and graphitization of bimetallic MOF-based composite, Chem 3 (2017) 152–163.
[28] J. Zhou, Z. Jiang, S. Niu, S. Zhu, J. Zhou, Y. Zhu, J. Liang, D. Han, K. Xu, L. Zhu, X. Liu, G. Wang, Y. Qian, Self-standing hierarchical P/CNTs@rGO with unprecedented capacity and stability for lithium and sodium storage, Chem 4 (2018) 372–385.
[29] B. Giri, M. Masroor, T. Yan, K. Kushnir, A.D. Carl, C. Doiron, H. Zhang, Y. Zhao, A. McClelland, G.A. Tompsett, D. Wang, R.L. Grimm, L.V. Titova, P.M. Rao, Balancing light absorption and charge transport in vertical SnS_2 nanoflake photoanodes with stepped layers and large intrinsic mobility, Adv Energy Mater 9 (2019) 1901236.
[30] Z. Khan, N. Parveen, S.A. Ansari, S.T. Senthilkumar, S. Park, Y. Kim, M.H. Cho, H. Ko, Three-dimensional SnS_2 nanopetals for hybrid sodium-air batteries, Electrochim Acta 257 (2017) 328–334.

[31] P.V. Prikhodchenko, D.Y.W. Yu, S.K. Batabyal, V. Uvarov, J. Gun, S. Sladkevich, A.A. Mikhaylov, A.G. Medvedev, O. Lev, Nanocrystalline tin disulfide coating of reduced graphene oxide produced by the peroxostannate deposition route for sodium ion battery anodes, J Mater Chem A 2 (2014) 8431.
[32] Y. Liu, A. Zhang, C. Shen, Q. Liu, J. Cai, X. Cao, C. Zhou, Single-step flash-heat synthesis of red phosphorus/graphene flame-retardant composite as flexible anodes for sodium-ion batteries, Nano Res 11 (2018) 3780–3790.
[33] H. Chen, B. Zhang, J. Zhang, W. Yu, J. Zheng, Z. Ding, H. Li, L. Ming, D.A.M. Bengono, S. Chen, H. Tong, In-situ grown SnS_2 nanosheets on rGO as an advanced anode material for lithium and sodium ion batteries, Front Chem 6 (2018) 629.
[34] L. Mei, C. Xu, T. Yang, J. Ma, L. Chen, Q. Li, T. Wang, Superior electrochemical performance of ultrasmall SnS_2 nanocrystals decorated on flexible RGO in lithium-ion batteries, J Mater Chem A 1 (2013) 8658.
[35] S.K. Park, Y.C. Kang, MOF-templated N-doped carbon-coated $CoSe_2$ nanorods supported on porous CNT microspheres with excellent sodium-ion storage and electrocatalytic properties, ACS Appl Mater Inter 10 (2018) 17203–17213.
[36] Y. Chen, B. Wang, T. Hou, X. Hu, X. Li, X. Sun, S. Cai, H. Ji, C. Zheng, Enhanced electrochemical performance of SnS nanoparticles/CNTs composite as anode material for sodium-ion battery, Chinese Chem Lett 29 (2018) 187–190.
[37] Q. Lu, X. Wang, J. Cao, C. Chen, K. Chen, Z. Zhao, Z. Niu, J. Chen, Freestanding carbon fiber cloth/sulfur composites for flexible room-temperature sodium-sulfur batteries, Energy Storage Mater 8 (2017) 77–84.
[38] L. Wang, C. Wang, N. Zhang, F. Li, F. Cheng, J. Chen, High anode performance of in situ formed Cu_2Sb nanoparticles integrated on Cu foil via replacement reaction for sodium-ion batteries, ACS Energy Lett 2 (2016) 256–262.
[39] X. Wang, X. Li, Q. Li, H. Li, J. Xu, H. Wang, G. Zhao, L. Lu, X. Lin, H. Li, S. Li, Improved electrochemical performance based on nanostructured SnS_2@CoS_2-rGO composite anode for sodium-ion batteries, Nano-micro Lett 10 (2018) 46.
[40] Y. Yan, Y.-X. Yin, Y.-G. Guo, L.-J. Wan, A sandwich-like hierarchically porous carbon/graphene composite as a high-performance anode material for sodium-ion batteries, Adv Energy Mater 4 (2014) 1301584.
[41] S. Wang, S. Liu, X. Li, C. Li, R. Zang, Z. Man, Y. Wu, P. Li, G. Wang, SnS_2/Sb_2S_3 heterostructures anchored on reduced graphene oxide nanosheets with superior rate capability for sodium-ion batteries, Chem Eur J 24 (2018) 3873–3881.
[42] X. Xie, D. Su, S. Chen, J. Zhang, S. Dou, G. Wang, SnS_2 nanoplatelet@graphene nanocomposites as high-capacity anode materials for sodium-ion batteries, Chem. Asian J. 9 (2014) 1611–1617.